ACS APPLIED NANO MATERIALS

www.acsanm.org Article

Magnetic Fe_3O_4 Nanocubes Coated with Silica and Nb-Doped TiO_2 for Recyclable Photocatalytic Degradation of Ciprofloxacin

Melissa Ariza Gonzalez, Minh Dang Nguyen, Quoc Minh Tran, Supawitch Hoijang, Pailinrut Chinwangso, Francisco C. Robles Hernandez, Debora F. Rodrigues,* and T. Randall Lee*

Cite This: *ACS Appl. Nano Mater.* 2025, 8, 22540−22552 Read Online

ACCESS | Metrics & More | Article Recommendations | Supporting Information

ABSTRACT: Antibiotics, recognized as "emerging contaminants", have been detected in increasing concentrations within aquatic ecosystems, contributing to elevated pollution levels and accelerating the development of antimicrobial resistance. Ciprofloxacin (CIP), one of the most prescribed antibiotics globally, exemplifies this challenge due to its persistence and resistance to conventional wastewater treatment methods. The inefficiency of existing water treatment approaches, often reliant on harmful chemical agents, exacerbates both health and environmental risks, underscoring the need for a sustainable, effective, and eco-friendly solution for antibiotic remediation. This study addresses this critical issue by synthesizing strongly magnetic iron oxide nanocubes (Fe_3O_4 NCs) coated with silica (SiO_2) and niobium-doped titanium dioxide (Nb-TiO_2)—Fe_3O_4@SiO_2@Nb-TiO_2—as a photocatalyst for CIP degradation under visible-light irradiation. The magnetic Fe_3O_4 core enables easy recovery and reuse of the nanoparticles (NPs), while Nb-TiO_2 doping improves photocatalytic performance by reducing the bandgap and extending light absorption into the visible spectrum. The intermediate SiO_2 shell mitigates interparticle interactions of the magnetic core and promotes the formation of a more crystalline TiO_2 structure. Results demonstrate that the synthesized NPs remove from 90 to 96% of CIP across initial concentrations of 5 to 40 ppm under visible light. The degradation followed pseudo-first-order kinetics, with the rate constant increasing as the initial CIP concentration decreased. The catalysts retained their activity over five reuse cycles, highlighting their durability and potential as a sustainable solution for antibiotic removal. This study emphasizes the integration of magnetic nanotechnology and photocatalysis as an innovative, recoverable, and environmentally friendly approach to water treatment, contributing to global efforts to safeguard public health and water resources.

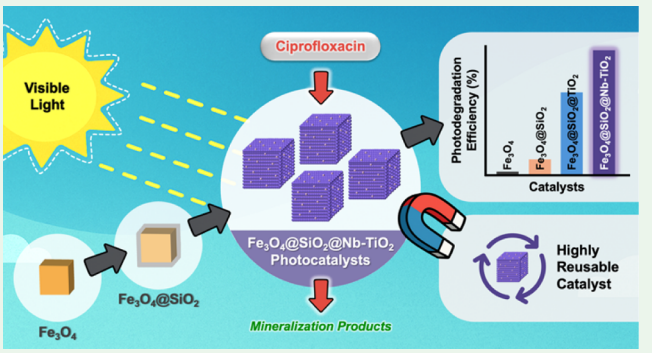

KEYWORDS: *nanomaterials, semiconductors, photocatalysis, water treatment, magnetic nanoparticles, niobium-doped titanium dioxide, antibiotic removal, ciprofloxacin*

INTRODUCTION

Water is a vital resource on Earth, essential for the survival of humans and other living organisms. It plays a crucial role in safe drinking, sanitation, agriculture, and maintaining a healthy ecosystem. However, the widespread production, consumption, and improper disposal of antibiotics have led to their persistent presence in water bodies, contributing to the global issue of antimicrobial resistance (AMR) and ecological imbalances.[1−3] Major contamination sources include industrial effluents, hospital and veterinary discharges, and wastewater from antibiotic consumption.[4,5] Even at low concentrations, antibiotics can disrupt aquatic ecosystems, harm biodiversity, and enter the food chain through irrigation, accelerating the spread of AMR and posing risks to human health.[6,7] The persistence of antibiotics in water has made them a critical emerging contaminant, posing serious ecological and public health implications.[8,9] Their prolonged presence in water sources facilitates the emergence of resistant bacterial strains, diminishing treatment efficacy, elevating healthcare costs, and contributing to rising global mortality rates.[10−13]

Ciprofloxacin (CIP) is among the most prescribed antibiotics worldwide and is widely used as an antibacterial agent against a broad spectrum of pathogens. It is used to treat various bacterial infections, including respiratory, urinary tract, gastrointestinal, and skin infections.[14,15] Due to its extensive use in human and veterinary medicine, along with its persistence and resistance to degradation in conventional

Received: June 30, 2025
Revised: October 21, 2025
Accepted: October 22, 2025
Published: November 18, 2025

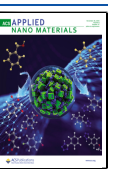

https://doi.org/10.1021/acsanm.5c03103
ACS Appl. Nano Mater. 2025, 8, 22540−22552

wastewater treatment processes, CIP is among the most commonly detected antibiotics in wastewater and natural water bodies.[16,17] The World Health Organization (WHO) recognizes both the importance of CIP and the threat of CIP resistance as critical public health concerns, highlighting the need for improved monitoring and removal strategies.[14,18] Existing water treatment processes are often unable to fully remove antibiotics from water and frequently rely on harmful chemicals that introduce additional health and environmental risks.[5,19] Developing sustainable, effective, and eco-friendly strategies for antibiotic removal is essential to safeguard water resources and address these risks.

Among emerging water treatment technologies, photocatalysis has shown significant promise for degrading persistent contaminants like CIP.[20−23] Titanium dioxide (TiO_2) is a widely studied photocatalyst due to its high photocatalytic degradation capacity, cost-effectiveness, environmental compatibility, and reusability.[24,25] However, its large bandgap (~3.2 eV) restricts its activity to ultraviolet (UV) light, which constitutes only ~5% of the solar spectrum, limiting its practical application.[26] To improve its photocatalytic efficiency, TiO_2 can be modified through metal or nonmetal doping, which extends light absorption into the visible range, reduces electron−hole recombination for the degradation of antibiotics in water.[27−29]

Magnetic nanoparticles (NPs), particularly iron oxide (Fe_3O_4)-based materials, offer an innovative approach for water treatment due to their ease of recovery using an external magnetic field.[30,31] Modifying these NPs with photocatalytic coating improves their performance, promoting dispersion and stability.[32] After pollutant degradation, magnetic separation simplifies photocatalyst recovery, reducing material use and eliminating energy-intensive techniques like filtration or centrifugation. Fe_3O_4 nanocubes (NCs) are promising for water purification due to their enhanced magnetic properties; they exhibit higher saturation magnetization than spherical particles, improving their efficiency in magnetic separation.[31,33,34] However, Fe_3O_4 NPs are prone to oxidation or degradation over time when exposed to oxygen, moisture, or acidic conditions, leading to a loss of magnetic properties and reduced performance.[35] Surface modifications can mitigate these effects, improving the stability and maximizing the functionalities of NPs. However, direct TiO_2 coating on Fe_3O_4 can facilitate charge transfer from the shell to the core, potentially causing the dissolution of iron ions into the solution, which might reduce photocatalytic activity.[36,37] To overcome these challenges, a silica (SiO_2) interlayer can be introduced to improve structural stability, prevent aggregation, and template a crystalline TiO_2 shell to enhance overall photocatalytic performance.[38,39] The incorporation of a nonmagnetic SiO_2 shell has been widely reported to reduce magnetic dipole−dipole interactions and limit agglomeration in magnetic NP systems, thereby enhancing colloidal stability.[40,41]

Incorporating a niobium-doped TiO_2 (Nb-TiO_2) shell layer onto the magnetic NPs provides a promising approach to improve photocatalytic performance and functional durability while facilitating catalyst recovery and recycling after use.[42] Nb doping not only decreases the rate of electron−hole recombination,[42,43] but also modifies TiO_2 surface properties by increasing surface area and active sites, thereby providing additional reactive sites for pollutant degradation.[44] Although Nb-TiO_2 has not been specifically tested for antibiotic degradation, it has been synthesized for applications such as carbon dioxide reduction,[45,46] hydrogen evolution,[42] organic compound degradation,[44,47] and photovoltaic applications.[48,49] This integration of Nb doping and magnetic recoverability creates a more sustainable and reusable photocatalyst, which is particularly advantageous for wastewater treatment applications.

Existing water treatment processes often fail to adequately remove antibiotics, relying on harmful chemicals that pose additional risks to health and the environment. Therefore, there is a pressing need to develop sustainable, effective, and eco-friendly approaches for antibiotic removal. This study addresses this challenge by synthesizing Fe_3O_4 NCs coated with SiO_2 and Nb-TiO_2 (Fe_3O_4@SiO_2@Nb-TiO_2) as a photocatalytic material to degrade CIP under visible-light exposure (see Scheme 1). The magnetic nature of the Fe_3O_4 core enables easy retrieval and reuse of NPs after treatment, while Nb doping in TiO_2 extends light absorption to the visible range by reducing the bandgap and enhancing light-harvesting capacity. This study aims to develop a safe and efficient approach for antibiotic remediation, prioritizing environmental sustainability and public health, and demonstrates the potential of integrating magnetic nanotechnology with photocatalysis for recoverable and effective and water treatment solutions.

Scheme 1. Schematic Representation of the Photocatalytic Degradation Process of Ciprofloxacin Using Fe_3O_4@SiO_2@Nb-TiO_2 NPs with an External Magnetic Source for Separation, Recovery, and Reuse

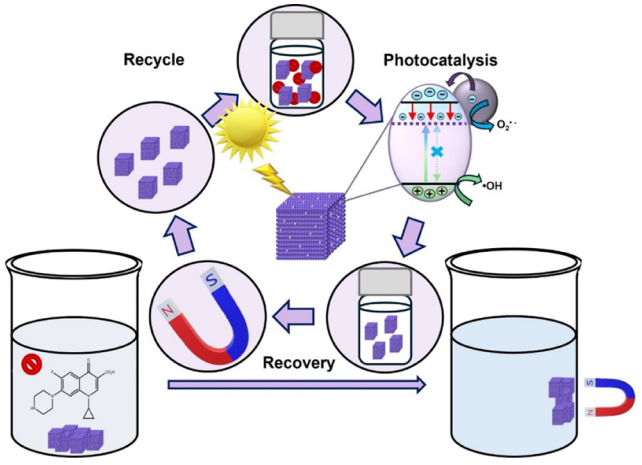

EXPERIMENTAL SECTION

Materials. Iron(III) acetylacetonate ($Fe(acac)_3$, 99%), benzyl ether (99%), oleic acid (90%), poly(oxyethylene)-nonylphenyl ether) (Igepal CO-520), cyclohexane (99%), tetraethyl orthosilicate (TEOS, 98%), hydroxypropyl cellulose (HPC, M_W ~ 100,000), titanium butoxide (TBOT, 97%), niobium(IV) ethoxide (NbOEt, 99%), and ciprofloxacin (CIP) were purchased from Sigma-Aldrich (USA). 4-Biphenylcarboxylic acid (99%) was obtained from Acros Organics (USA, now Thermo Scientific Chemicals, USA). Ammonium hydroxide (28−30%) was sourced from VWR Chemicals BDH (USA). Ethanol was purchased from Koptec (USA). Water was purified to a resistance of 18 MΩ-cm, employing an Academic Milli-Q Water System (Millipore Corporation) and filtered through a 0.22 μm membrane before use. All glassware used in

https://doi.org/10.1021/acsanm.5c03103
ACS Appl. Nano Mater. 2025, 8, 22540−22552

Scheme 2. Step-by-Step Schematic Representation of the Synthesis of Fe_3O_4@SiO_2@Nb-TiO_2 NPs

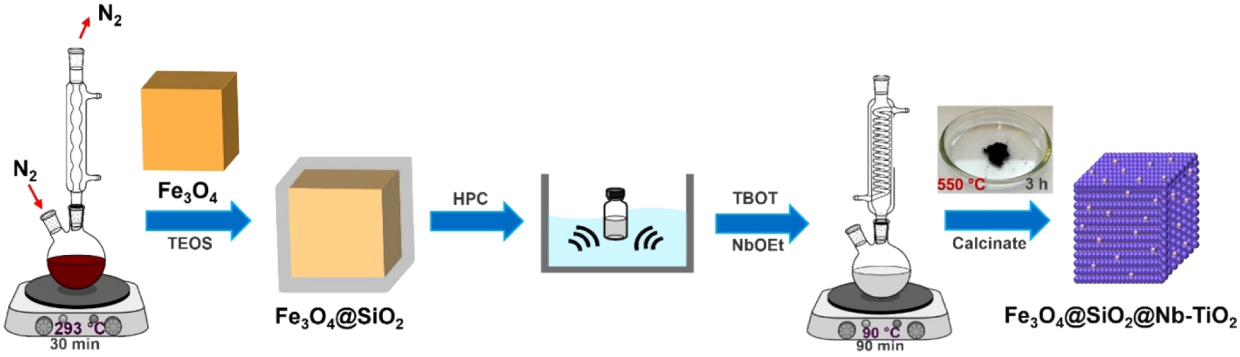

the experiments was cleaned with piranha solution (3:1 H_2SO_4:H_2O_2) and aqua regia solution (3:1 HCl:HNO_3) prior to use.

Synthesis of Size-Controlled Fe_3O_4 Nanocubes. Magnetic Fe_3O_4 NCs were synthesized using a modified version of the method reported by Kim and coworkers, involving the thermal decomposition of $Fe(acac)_3$.[50] In a typical synthesis procedure, 0.706 g of $Fe(acac)_3$ and 0.4 g of 4-biphenylcarboxylic acid were added to a 100 mL two-neck round-bottom flask, followed by the addition of a mixture of 1.14 g of oleic acid and 16 mL of benzyl ether. The solution was degassed under a nitrogen atmosphere for 1 h at room temperature while being stirred by magnetic stir bar to dissolve the precursors. The reaction mixture was then heated to 293 °C and maintained at this temperature for 30 min. The Fe_3O_4 NCs were collected using a magnet, washed thoroughly with ethanol and then Milli-Q water, and dried at 60 °C overnight.

Synthesis of Fe_3O_4@SiO_2 Nanoparticles. To coat the magnetic Fe_3O_4 NCs with Nb-TiO_2, a SiO_2 shell was deposited to prevent electronic interaction and corrosion of the core, as well as to facilitate crystallization of the photocatalyst. The core−shell Fe_3O_4@SiO_2 NPs were synthesized using a modified version of the reverse microemulsion method previously reported.[51] Oleic acid-stabilized Fe_3O_4 NCs (22 mg) were dispersed in 8.8 mL of cyclohexane under ultrasonication for 45 min and then transferred to a 40 mL vial. Separately, 1.0 g of Igepal CO-520 was dissolved in 22 mL of cyclohexane, sonicated for 10 min to form a homogeneous suspension, and subsequently combined with the Fe_3O_4 dispersion. To this mixture, 200 μL of ammonium hydroxide was added, followed by the dropwise addition of 150 μL of TEOS. The resulting mixture was stirred continuously for 24 h at room temperature. The Fe_3O_4@SiO_2 NPs were isolated using a magnetic separator, washed thoroughly with ethanol and Milli-Q water to remove residual surfactants, and redispersed in Milli-Q water.

Synthesis of Fe_3O_4@SiO_2@Nb-TiO_2 Nanoparticles. The Fe_3O_4@SiO_2@Nb-TiO_2 NPs were synthesized using a two-step procedure following the method described by Lee and coworkers.[52] In the first step, the Fe_3O_4@SiO_2 NPs were functionalized with HPC. Initially, 44 mg of Fe_3O_4@SiO_2 NPs were dispersed in 10 mL of Milli-Q water with sonication for 30 min. Subsequently, 26 mg of HPC was added to the suspension for functionalization, followed by an additional 60 min of sonication. The solution was centrifuged to remove residual water, and the NPs were redispersed in ethanol. An additional 26 mg of HPC and 400 μL of Milli-Q water were added to the suspension, and the mixture was sonicated for 90 min. In the second step, the solution was transferred to a 100 mL round-bottom flask and stirred vigorously at room temperature to form a homogeneous dispersion. The precursor solution, containing a mixture of TBOT and NbOEt in ethanol, was then added dropwise to the dispersion, and the reaction was stirred continuously overnight at room temperature. Following this, the mixture was refluxed at 90 °C for 90 min. The resulting product was centrifuged, washed with ethanol, and dried in an oven at 60 °C overnight. The dried powder was then calcined at 550 °C for 3 h. For the control study, Fe_3O_4@SiO_2@TiO_2 NPs (i.e., without Nb doping) were synthesized using the same procedure as described earlier, except that NbOEt was omitted from the precursor solution. The synthesis process is illustrated in detail in Scheme 2, which provides a step-by-step schematic representation of the preparation of Fe_3O_4@SiO_2@Nb-TiO_2 NPs.

Characterization Methods. The lower magnification imaging was performed using a JEM-2010 FX transmission electron microscope (TEM) operating at 200 kV. The scanning transmission electron micrographs (STEM), high-angle annular dark-field (HAADF) imaging, high resolution transmission electron microscopy (HRTEM), and energy dispersive X-ray spectroscopy (EDS) maps were obtained by using the FEI Titan Themis3 system equipped with image and probe aberration corrections and an electron monochromator at 300 kV. TEM samples were prepared by depositing the NPs on 200-mesh holey carbon-coated copper grids. X-ray diffraction (XRD) analysis was conducted using a diffractometer with Cu Kα radiation (λ = 1.540562 Å) over a 2θ range of 5−80°. X-ray photoelectron spectroscopy (XPS) analysis was carried out using a PHI 5700 X-ray photoelectron spectrometer equipped with a monochromatic Al Kα source with 10 mA emission current and 15 kV emission bias; all spectra were calibrated using the C 1s peak at 284.8 eV. Magnetic properties were measured at 300 K using a vibrating sample magnetometer (LakeShore VSM 7300 Series) equipped with a LakeShore 735 Controller and a LakeShore 450 Gmeter. Photoluminescence (PL) measurements were performed using a PerkinElmer LS-55 fluorescence spectrometer to evaluate the electron−hole recombination rate of the semiconductor nanostructures. The detection and quantification of trace elements during dissolution and photodissolution experiments were performed using inductively coupled plasma mass spectrometry (ICP−MS). Diffuse reflectance spectra (DRS) were recorded for all crystalline NP samples using a V-770 UV−vis−near-infrared spectrophotometer (Jasco, Inc.). The removal efficiency of CIP was determined by measuring

https://doi.org/10.1021/acsanm.5c03103
ACS Appl. Nano Mater. 2025, 8, 22540−22552

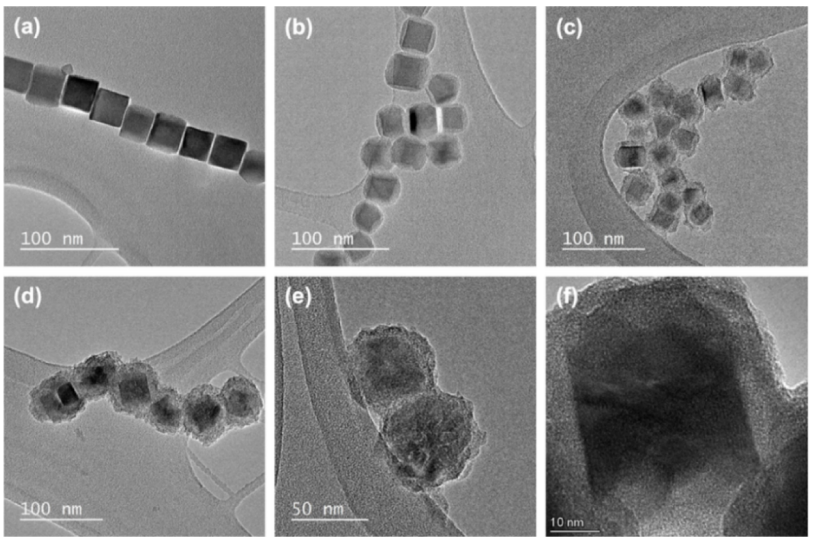

Figure 1. TEM images of (a) Fe_3O_4 NCs, (b) Fe_3O_4@SiO_2 NPs, and (c–f) Fe_3O_4@SiO_2@Nb-TiO_2 NPs.

absorbance values using a UV–vis spectrophotometer and a SynergyMX microtiter plate reader (Biotek).

Photocatalytic Experiments. The photocatalytic performance of Fe_3O_4@SiO_2@TiO_2 NPs (denoted as undoped NPs) and Fe_3O_4@SiO_2@Nb-TiO_2 NPs (denoted as doped NPs) was evaluated for the degradation of CIP under visible light irradiation using an LED light source with a wavelength of 460 nm. A 120 cm LED strip (14.4 W/m) was wrapped around a 200 mL quartz flask. The estimated light intensity at the sample surface was ~86 mW cm^{-2}. Prior to photocatalysis, 15 mL of CIP solutions (5–40 ppm) with 100 mg of NPs were stirred in the dark for 30 min to establish adsorption–desorption equilibrium on the surface of the NPs, ensuring optimal photocatalytic efficiency and stability. Each experiment was conducted using a 20 mL glass vial. For each CIP concentration, a control without NPs and a vial covered with aluminum foil to prevent light interactions with CIP and NPs were included, along with three replicates of the CIP-NPs vials. The photocatalytic reaction was initiated under visible light while continuously stirring to maintain the suspension of the photocatalyst. At predetermined time intervals, 300 μL of the mixture were withdrawn, and the photocatalyst was magnetically separated from the solution. The remaining solution was analyzed using a UV–vis spectrophotometer. The reaction was monitored every 20 min until the contaminant concentration stabilized, indicating the maximum removal efficiency. The extent of CIP degradation was quantified by measuring the absorbance values on a UV–vis spectrophotometer, and a normalized plot of CIP concentration versus time was generated to illustrate the degradation profile. The photodegradation efficiency of CIP, expressed as percentage, was calculated using eq 1:

$$\text{Photodegradation of CIP (\%)} = [(C_0 - C)/C_0] \times 100 \quad (1)$$

where C_0 and C represent the concentrations of CIP (ppm) at initial state and time t (i.e., at different time intervals of visible light irradiation), respectively. To facilitate comparative analysis, CIP photodegradation kinetics were evaluated using the pseudo-first-order kinetics model, as described in eq 2:

$$-\ln(C/C_0) = kt \quad (2)$$

where k is the pseudo-first-order rate constant (min^{-1}) and t represents the reaction time.

Stability Tests of Nanoparticles: Ion Dissolution under Light and pH Conditions. The stability of the NPs was evaluated across a range of pH values (3, 5, 7, 10, and 13) to study ion dissolution behavior on both doped and undoped catalyst materials. Milli-Q water was adjusted to the desired pH using 0.1 M HCl and 0.1 M NaOH. Subsequently, the doped and undoped NPs (100 mg) were introduced into these pH-adjusted solutions, mixed, and stirred at room temperature. After 24 h, the samples were separated using an external magnet, filtered through a 0.2 μm syringe filter (VWR sterile syringe filter), and centrifuged to remove any residual NPs. For photodissolution testing, the NPs were dispersed in pH-adjusted solutions and exposed to visible light for 24 h with vigorous stirring to ensure proper suspension. Following the dissolution and photodissolution procedures, the resulting solutions were analyzed using ICP–MS to quantify iron, titanium, and niobium ion concentrations. Each condition was analyzed in triplicate to ensure reproducibility. For ICP–MS calibration, standard solutions of iron, titanium, and niobium were prepared at concentrations of 1, 5, 10, 15, and 20 ppm to ensure accurate quantification.

Reusability Test of Nanoparticles. The reusability and removal efficiency of Fe_3O_4@SiO_2@Nb-TiO_2 NPs were evaluated through photocatalytic treatment under visible light for CIP degradation. After each cycle of contaminant removal, the NPs were rinsed thoroughly with Milli-Q water to recover the photocatalyst for subsequent use. Removal efficiency was measured at the end of each cycle. For consistency, a freshly prepared CIP solution with the same initial concentration (30 ppm) was used in each cycle, with three replicates. This process was repeated over multiple cycles to assess the reusability and long-term stability of the photocatalyst.

RESULTS AND DISCUSSION

Morphology, Structure, and Size of Nanoparticles. The morphology, structure, and size of the synthesized NPs were characterized using TEM. Representative TEM images illustrating each synthesis step are presented in Figure 1. In Figure 1a, Fe_3O_4 NCs exhibit uniform cubic morphologies. The encapsulation of these Fe_3O_4 NCs within a smooth,

https://doi.org/10.1021/acsanm.5c03103
ACS Appl. Nano Mater. 2025, 8, 22540–22552

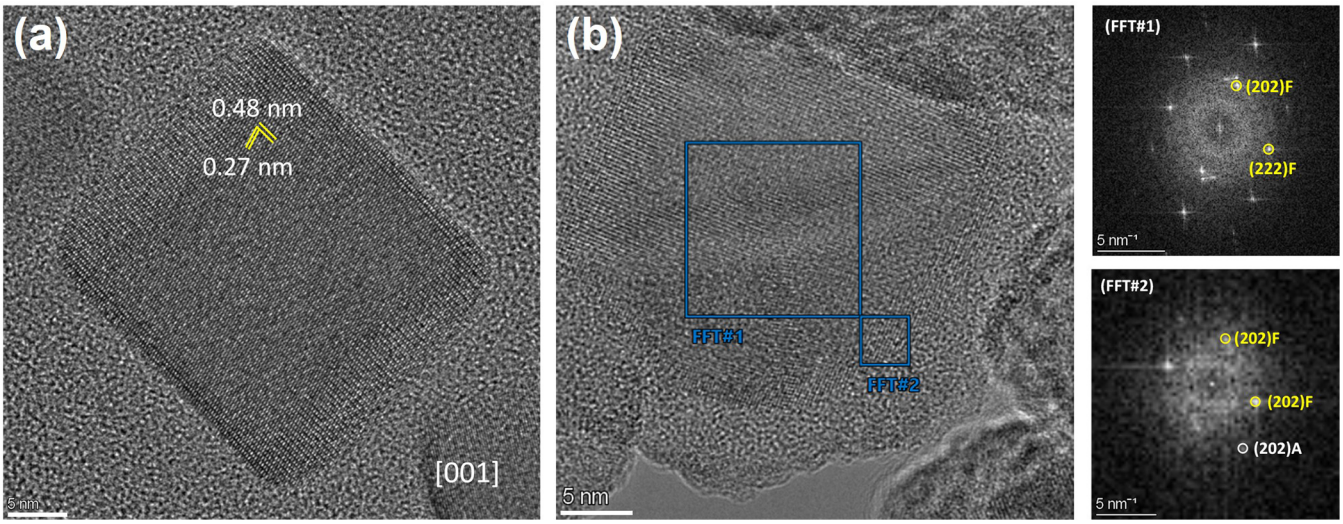

Figure 2. HRTEM images and FFT simulated diffraction patterns of the NPs, highlighting structural and compositional details. (a) shows the as-synthesized Fe_3O_4 NP, with the inset confirming the exclusive presence of Fe_3O_4 through its FFT diffraction pattern. (b) displays a composite NP, where region (FFT#1) reveals Fe_3O_4 and (FFT#2) shows the presence of both Fe_3O_4 and TiO_2, indicating the core−shell structure. The FFT diffraction patterns in the insets further support this analysis, with planes labeled as "F" for Fe (iron) and "A" for anatase, demonstrating the successful synthesis and structural integration of the composite material.

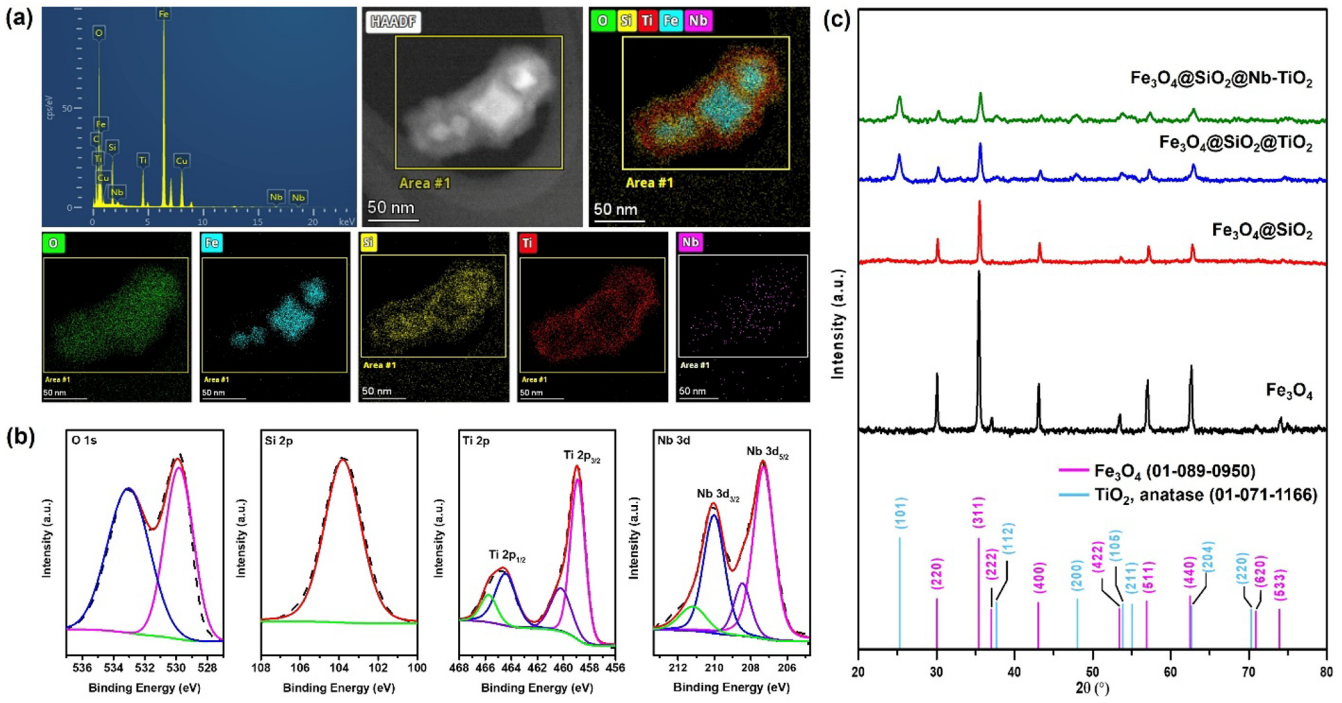

Figure 3. (a) HAADF image of the Fe_3O_4@SiO_2@Nb-TiO_2 NPs with corresponding STEM-EDS spectrum and elemental maps showing the spatial distribution of Fe, Si, Ti, O, and Nb. (b) High-resolution XPS spectra of O 1s, Si 2p, Ti 2p, and Nb 3d for Fe_3O_4@SiO_2@Nb-TiO_2 NPs. (c) XRD spectra of Fe_3O_4, Fe_3O_4@SiO_2, Fe_3O_4@SiO_2@TiO_2, and Fe_3O_4@SiO_2@Nb-TiO_2 NPs.

spherical silica SiO_2 is evident in Figure 1b. The final product, Fe_3O_4@SiO_2@Nb-TiO_2 NPs, is shown in Figure 1c−f, where a Nb-TiO_2 layer can be observed as a coating on the SiO_2 shell. The distinct layers surrounding the Fe_3O_4 NCs confirm the successful formation of the composite structure. It is noteworthy that the Nb-TiO_2 layer appears less uniform, likely due to the inherent porosity of the TiO_2 matrix. To assess particle size distribution at each synthesis stage, TEM images of approximately 150 NPs were analyzed (Figure S1). The Fe_3O_4 NCs exhibited a monodisperse average particle size (i.e., the edge length) of ∼28 ± 2 nm. The addition of the SiO_2 shell increased the average particle size to ∼36 ± 2 nm, while the subsequent deposition of the Nb-TiO_2 coating further increased the average particle size to ∼42 ± 4 nm.

The HRTEM images in Figure 2 illustrate the Fe_3O_4 NCs in their as-synthesized form and as a composite with a Nb-TiO_2 coating layer. Figure 2a highlights two key observations. First, it reveals the Fe_3O_4 NP with a characteristic lattice spacing of 0.48 nm, which is consistent with the (111) plane of the inverse spinel cubic structure commonly described by the

https://doi.org/10.1021/acsanm.5c03103
ACS Appl. Nano Mater. 2025, 8, 22540−22552

$Fd\bar{3}m$ space group. The surface shown in Figure 2a corresponds to the ⟨100⟩ crystallographic plane family, as do the other visible facets, indicating that the crystal is oriented along the [001] zone axis. The second observation pertains to the size disparity between the bare NPs and the composite NPs, clearly demonstrating an increase in size due to the coating layers. This size enhancement is consistent with the statistical analysis presented. Figure 2b depicts the composite NP, where the core remains Fe_3O_4 (FFT#1), and the shell predominantly consists of TiO_2 (FFT#2) in the anatase phase. The core region exhibits structural features indicative of both materials contributing to the composite, while the outer edges are primarily composed of TiO_2. The identification of SiO_2 within the composite is challenging due to its relatively lower abundance and amorphous nature. The difficulty in detecting SiO_2 can be attributed to its possible presence as short-range domains or in an amorphous state, rendering its structural identification complex. Conversely, the presence of TiO_2 in the anatase phase is evident, and analysis of the planes in Figure 2b enables the successful identification of the $I4_1/amd$ space group characteristic of anatase.

Chemical Composition and Crystallographic Structures of Nanoparticles. The chemical composition and elemental distribution of the Fe_3O_4@SiO_2@Nb-TiO_2 NPs were analyzed using TEM equipped with STEM-EDS. As shown in Figure 3a, the STEM-EDS spectrum confirms the presence of all expected elements—iron (Fe), silicon (Si), titanium (Ti), niobium (Nb), and oxygen (O)—indicating the successful synthesis of the core−shell structure. In addition, the elemental mapping illustrates the spatial distribution of these elements, confirming the core−shell structure of the composite. The Fe signal corresponds to the Fe_3O_4 magnetic core, while Si signal highlights the uniform SiO_2 intermediate layer. The Ti and Nb signals verify the incorporation of Nb into the TiO_2 shell, supporting the formation of designed structure. The O distribution is consistent with the composite stoichiometry, enveloping the nanostructure and affirming its structural integrity. Notably, the Nb map reveals low-concentration domains, indicative of single or few-atom clusters, which are characteristic of dopants, further validating the successful doping of the TiO_2 shell. The corresponding elemental weight percentages obtained from EDS analysis are provided in Table S1.

XPS was used to analyze the elemental composition, chemical states, and incorporation of Nb into the TiO_2 lattice in Fe_3O_4@SiO_2@Nb-TiO_2 NPs. The survey XPS spectra (Figure S2) revealed the presence of O, Si, Ti, and Nb, consistent with the EDS data, confirming the successful deposition of these elements on the sample surface. High-resolution XPS spectra provided detailed insights into the chemical states of O 1s, Si 2p, Ti 2p, and Nb 3d, as shown in Figure 3b.

Analysis of the O 1s spectrum provided further insight into the surface chemistry of the NPs. Two main contributions were identified: lattice oxygen (O−Ti or O−Nb) at ∼530.2 eV, and surface peroxo (O−O) species at ∼533.0 eV, the latter being more prevalent in the Nb-doped NPs. The formation of peroxo species is expected under wet-chemistry-synthesis conditions,[47] arising from the substitution of terminal −OH groups and remaining structurally stable under catalytic conditions.[53] Their presence promotes partial electron transfer from metal centers (Ti, Nb) to O−O groups, thereby decreasing metal electron density.[54] This additional surface chemical environment likely contributes to the emergence of two distinct Ti^{4+} and Nb^{5+} states in the doped NPs.

The Si 2p spectrum displayed a peak at 103.7 eV, confirming the presence of SiO_2. The Ti 2p spectrum exhibited Ti $2p_{3/2}$ and Ti $2p_{1/2}$ peaks at 457.7 and 463.2 eV, respectively, which are characteristic of Ti^{4+} in TiO_2 for the undoped Fe_3O_4@SiO_2@TiO_2 sample. Deconvolution of the Ti 2p spectrum, for the Fe_3O_4@SiO_2@Nb-TiO_2 sample, revealed two sets of Ti^{4+} species: the first at 458.9 eV (Ti $2p_{3/2}$) and 464.5 eV (Ti $2p_{1/2}$), corresponding to stoichiometric TiO_2, and the second at 460.2 eV (Ti $2p_{3/2}$) and 465.7 eV (Ti $2p_{1/2}$), attributed to Nb-induced modifications in the Ti^{4+} chemical environment or altered surface coordination, both of which reduce electron density around Ti.[55] Relative with the undoped Fe_3O_4@SiO_2@TiO_2 sample (Figure S3) the Nb-doped NPs exhibit a slight positive shift in Ti binding energies. This shift is ascribed to substitutional Nb^{5+} incorporation into the anatase lattice, where the higher electronegativity of Nb promotes electron withdrawal from adjacent Ti atoms, thereby decreasing Ti electron density. The emergence of an additional, more oxidized Ti species likely arises from variations in local chemical environments, consistent with the presence of two Nb coordination environments.

Furthermore, the Nb 3d spectrum displayed peaks at 210.3 and 207.6 eV, corresponding to Nb $3d_{3/2}$ and Nb $3d_{5/2}$, respectively, indicative of Nb in the pentavalent oxidation state (Nb^{5+}). Deconvolution of the Nb 3d spectrum revealed two doublets. The first set at 207.3 eV (Nb $3d_{5/2}$) and 210.0 eV (Nb $3d_{3/2}$), and the second at 208.5 eV (Nb $3d_{5/2}$) and 211.2 eV (Nb $3d_{3/2}$), both consistent with Nb^{5+} in slightly different coordination environments. The binding energy separation between these Nb environments (1.2 eV) is comparable to that observed for the two Ti environments (1.3 eV), suggesting a common structural origin. This similarity can be attributed to the slightly larger ionic radius of Nb^{5+} (0.640 Å) relative to that of Ti^{4+} (0.605 Å), which can induce lattice strain, promote formation of structural defects, and generate unsaturated metal coordination sites or surface peroxo-based species, as discussed.

The results above confirm the substitution of Ti^{4+} ions by Nb^{5+} ions within the TiO_2 lattice, facilitated by their similar ionic radii and charges, enabling the formation of a solid solution within the anatase structure. The combined effects of lattice distortion, defect generation, and peroxo-induced electronic modification provide a coherent rationalization for the observed binding energy shifts and the coexistence of multiple Nb and Ti chemical environments. These findings are consistent with previously reported studies.[44,47,55,56]

The crystal structure and composition of the NPs were characterized using XRD, as shown in Figure 3c. The distinctive diffraction peaks observed for Fe_3O_4@SiO_2@Nb-TiO_2 illustrate the high crystallinity of the composite material. The Fe_3O_4 NPs exhibited an inverse spinel ferrite structure, with diffraction peaks indexed to the (220), (311), (222), (400), (422), (511), (440), and (533) planes at 2θ values of 30.2°, 35.5°, 37.2°, 43.2°, 53.6°, 57.1°, 62.7°, and 74.2°, respectively, consistent with JCPDS card no. 01-089-0950. After SiO_2 coating, no significant structural changes were observed, although a reduction in the relative crystallinity was noted, likely due to the presence of amorphous SiO_2, consistent with the TEM observations. The deposition of TiO_2 introduced additional diffraction peaks at 2θ values of 25.2°, 38.5°, 47.9°, and 54.9°, corresponding to the anatase

https://doi.org/10.1021/acsanm.5c03103
ACS Appl. Nano Mater. 2025, 8, 22540−22552

(101), (112), (200), and (211) planes, respectively, as identified by JCPDS card no. 01-071-1166. The Fe_3O_4 peaks at 2θ values of 35.5°, 43.2°, 57.1°, and 62.7° remained prominent, exhibiting the successful incorporation of TiO_2 onto the Fe_3O_4 magnetic core. Nb doping in the TiO_2 shell led to broadening of the characteristic anatase peak at 25°, suggesting reduced crystallite size or increased lattice disorder, consistent with structural modifications induced by Nb incorporation. Despite these changes, the composite retained its crystalline nature, indicating that Nb incorporation did not disrupt the overall structural integrity of the material.

Building on the important role of the SiO_2 interlayer in enhancing TiO_2 crystallinity, a comparative analysis was performed using dual-shell NPs synthesized with and without this intermediate layer. This approach enabled a controlled assessment of the interlayer's influence on TiO_2 crystallization behavior. As demonstrated (Figure S4), direct deposition of TiO_2 onto Fe_3O_4 cores led to an amorphous coating, even after calcination. In contrast, introducing the SiO_2 interlayer markedly enhanced the formation of a crystalline TiO_2 shell. XRD data (Figure S4a) further emphasizes the interlayer's crucial role in enabling crystallinity, irrespective of doping. This effect was observed consistently in both doped and undoped NPs. Additionally, TEM and STEM-EDS analyses (Figure S4b and S4c) of TiO_2 shells deposited directly on bare Fe_3O_4 cores, for both doped and undoped samples, confirmed that while TiO_2 deposition is feasible without the SiO_2 interlayer, the resulting shell remains amorphous. Collectively, these results highlight the crucial role of the SiO_2 interlayer in facilitating the crystallization of TiO_2 within the dual-shell NP structures.

Magnetic Properties of Nanoparticles. The magnetic properties of the synthesized NPs, one of the most critical features of these materials for their application, were evaluated using VSM to measure the magnetic moment and coercivity as a function of the applied magnetic field. The resulting hysteresis loops, which illustrate the relationship between material magnetization and the applied magnetic field,[57] are presented in Figure 4. The magnetization curves for Fe_3O_4, Fe_3O_4@SiO_2, Fe_3O_4@SiO_2@TiO_2, and Fe_3O_4@SiO_2@Nb-TiO_2 NPs exhibit ferrimagnetic behavior, which remains preserved in the Fe_3O_4 cores despite successive coatings with SiO_2 and TiO_2. Under an external magnetic field, the NPs demonstrated a strong magnetic response. The saturation magnetization (M_S) value of Fe_3O_4 nanocrystals was recorded at 73 emu/g. Coating with an amorphous SiO_2 layer reduced the M_S to 41 emu/g, while subsequent coatings with TiO_2 and Nb-TiO_2 layers further reduced in M_S to 22 emu/g and 19 emu/g, respectively. These reductions are attributed to the nonmagnetic nature of the SiO_2 and TiO_2 coatings, which increase the nonmagnetic volume of the NPs, thus reducing the overall M_S value of dual shell NPs.

To maintain highly magnetic NPs after coating with dual shells of nonmagnetic materials, ferromagnetic Fe_3O_4 was selected for its higher M_S, ensuring sufficient response. The superparamagnetic cores would give low saturation magnetization, but effective separation would be reduced after forming dual-shell nanostructures. The particle size (~28 nm) is near the superparamagnetic to ferromagnetic transition size, leading to minimum coercivity and remnant magnetization, which minimizes agglomeration or magnetic-induced clusterings while supporting rapid magnetic response.[31,58] Despite these reductions, the Fe_3O_4@SiO_2@Nb-TiO_2 NPs retained ferri-

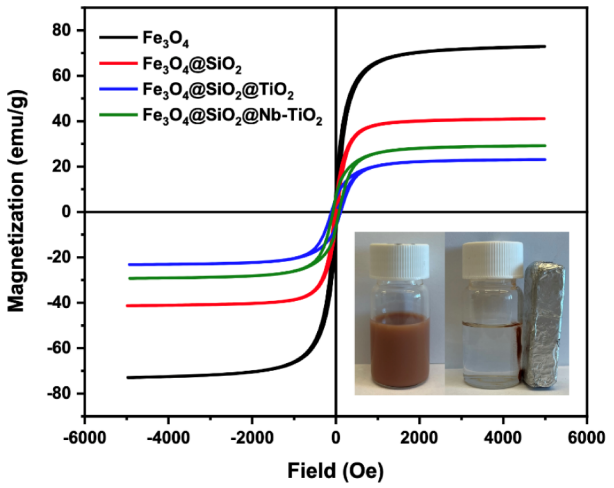

Figure 4. Hysteresis loops recorded at each synthesis stage for Fe_3O_4, Fe_3O_4@SiO_2, Fe_3O_4@SiO_2@TiO_2, and Fe_3O_4@SiO_2@Nb-TiO_2 NPs, showing the changes in magnetic properties as successive coating layers were added. The inset image demonstrates the efficient separation of the NPs using an external magnet, highlighting their retained magnetic responsiveness despite the addition of encapsulating layers.

magnetic behavior, allowing rapid response to an external magnetic field. This characteristic facilitates efficient separation of the NPs from the solution during photocatalytic processes, emphasizing the practicality of these materials in such applications.

Optical Behavior of Nanoparticles. PL spectroscopy, which measures the energy of emitted photon during electron−hole recombination, provides insights into the recombination behavior of photoinduced charge carriers. Higher PL intensity typically corresponds to a higher rate of electron−hole recombination.[59,60] Figure 5 illustrates the optical properties of the synthesized NPs. As shown in Figure 5a, the PL intensity decreases with the incorporation of Nb into TiO_2, indicating that Nb doping effectively suppresses electron−hole recombination and suggesting more efficient charge separation and extended carrier lifetimes, both of which are essential for enhancing photocatalytic activity.[61] The suppression facilitates the generation of oxidized and reduced radicals, thereby improving photocatalytic performance under visible light.[44] Notably, both doped and undoped NPs exhibits the same PL peak position at 445 nm, indicating that the primary emission pathway in TiO_2 is preserved upon Nb incorporation, while the reduced intensity reflects suppressed electron−hole recombination. These observations are consistent with previous reports showing that Nb doping reduces PL intensity by lowering the density of recombination centers, thereby improving photocatalytic efficiency.[42] These findings demonstrate that Nb doping not only reduces the electron−hole recombination rate but also facilitates electron transfer, thereby improving photocatalytic activity.

The solid-state diffuse reflectance spectra of Nb-doped and undoped Fe_3O_4@SiO_2@TiO_2 NPs, along with commercial TiO_2, are shown in Figure 5b. The corresponding Tauc plots in Figure 5c are used to estimate their optical bandgap energies. The bandgap energies of the Nb-doped and undoped Fe_3O_4@SiO_2@TiO_2 NPs were determined to be 2.79 and 2.90 eV, respectively, consistent with previous reports.[47,62] These values are significantly lower than that of the commercial TiO_2 (3.22

https://doi.org/10.1021/acsanm.5c03103
ACS Appl. Nano Mater. 2025, 8, 22540−22552

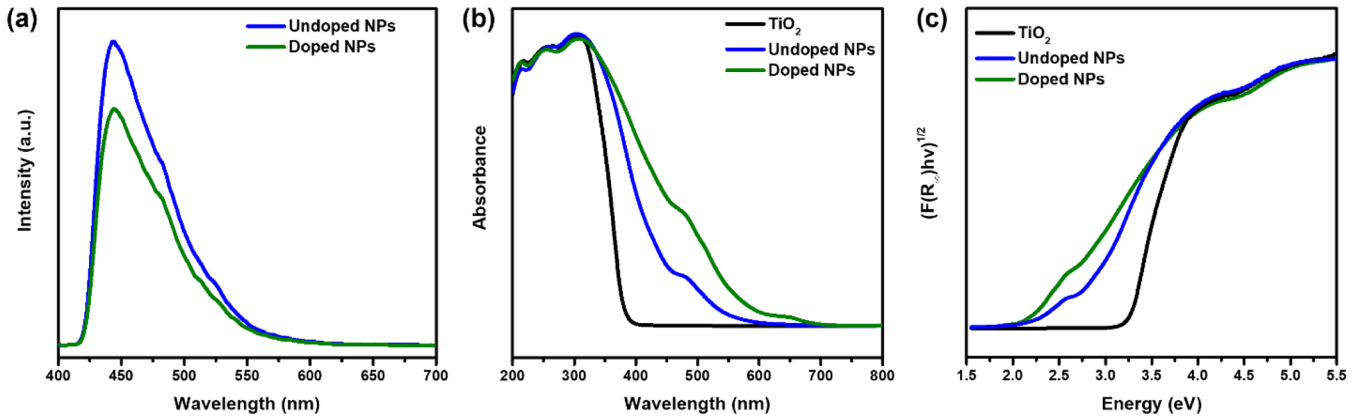

Figure 5. (a) PL spectra for Nb-doped and undoped Fe_3O_4@SiO_2@TiO_2 NPs. (b) Solid-state diffuse reflectance spectra and (c) Tauc plots of Nb-doped and undoped Fe_3O_4@SiO_2@TiO_2 NPs, compared to commercial TiO_2.

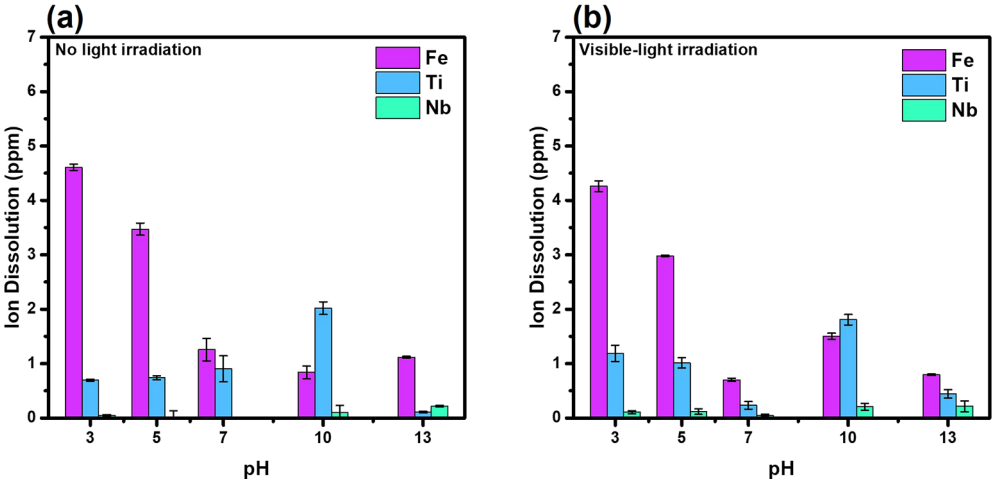

Figure 6. Ion dissolution behavior of Fe_3O_4@SiO_2@Nb-TiO_2 NPs in (a) the absence and (b) the presence of visible-light irradiation with different solution pH levels.

eV), indicating the promising photocatalytic potential of the synthesized materials under visible light irradiation. The bandgap values were obtained from reflectance spectra transformed using the Kubelka–Munk function, followed by Tauc-plot analysis and linear fitting, as described by Makula et al.[63] This approach enabled the resolution of distinct optical transitions, which were fitted using a baseline method. The corresponding transformed reflectance spectra and fitting plots for the observed transitions are presented (Figure S5) for both undoped and doped NPs.

The reduced bandgap in the undoped sample compared to commercial TiO_2 can be attributed to differences in crystallinity, particle size, and interface effects introduced by the Fe_3O_4 and SiO_2 layers. To clarify the contribution of Fe_3O_4 to the overall optical response, the DRS of bare Fe_3O_4, Fe_3O_4@SiO_2, and the TiO_2-based core–shell NPs are provided (Figure S5). This comparison allows for a clearer distinction between the optical behavior of the core materials and the TiO_2 shell, supporting the interpretation that the enhanced visible-light absorption and reduced bandgap are primarily influenced by the TiO_2 layer and its interaction with Nb dopants rather than the underlying structure.[50]

The Nb-doped NPs exhibited a substantial improvement in light absorption within the visible spectrum, as observed in the broaden absorption spectrum attributed to the incorporation of Nb ions. This doping effectively narrowed the bandgap of TiO_2, shifting its bandgap to lower energy window and extending the absorption range. The bandgap reduction demonstrates Nb^{5+} incorporation into the TiO_2 lattice, which modifies the optical properties of the material. Both Nb-undoped and doped Fe_3O_4@SiO_2@TiO_2 NPs exhibited reduced bandgaps compared to the commercial TiO_2, affirming the advantages of the composite structure. The enhanced photocatalytic activity can be attributed to the effective separation of photogenerated electron–hole pairs, as corroborated by the PL spectra. These results highlight the capability of Nb doping and composite design to engineer the optical bandgap and enhance the catalytic performance of the material for applications under visible light irradiation.

Ion Dissolution of Nanoparticles: pH and Light Stability. The application of many metal oxide nanomaterials is often constrained by dissolution, which can enhance toxicity and limit their utility.[64] This challenge is particularly pronounced in photocatalytic processes, where corrosion and degradation compromise long-term efficiency.[65,66] Dissolution and photodissolution experiments performed prior to photodegradation studies demonstrated that ionic dissociation is minimally influenced by the pH of the solution and has little impact on the surface properties or photocatalytic performance of the materials. A preliminary test after 12 h indicated no

https://doi.org/10.1021/acsanm.5c03103
ACS Appl. Nano Mater. 2025, 8, 22540–22552

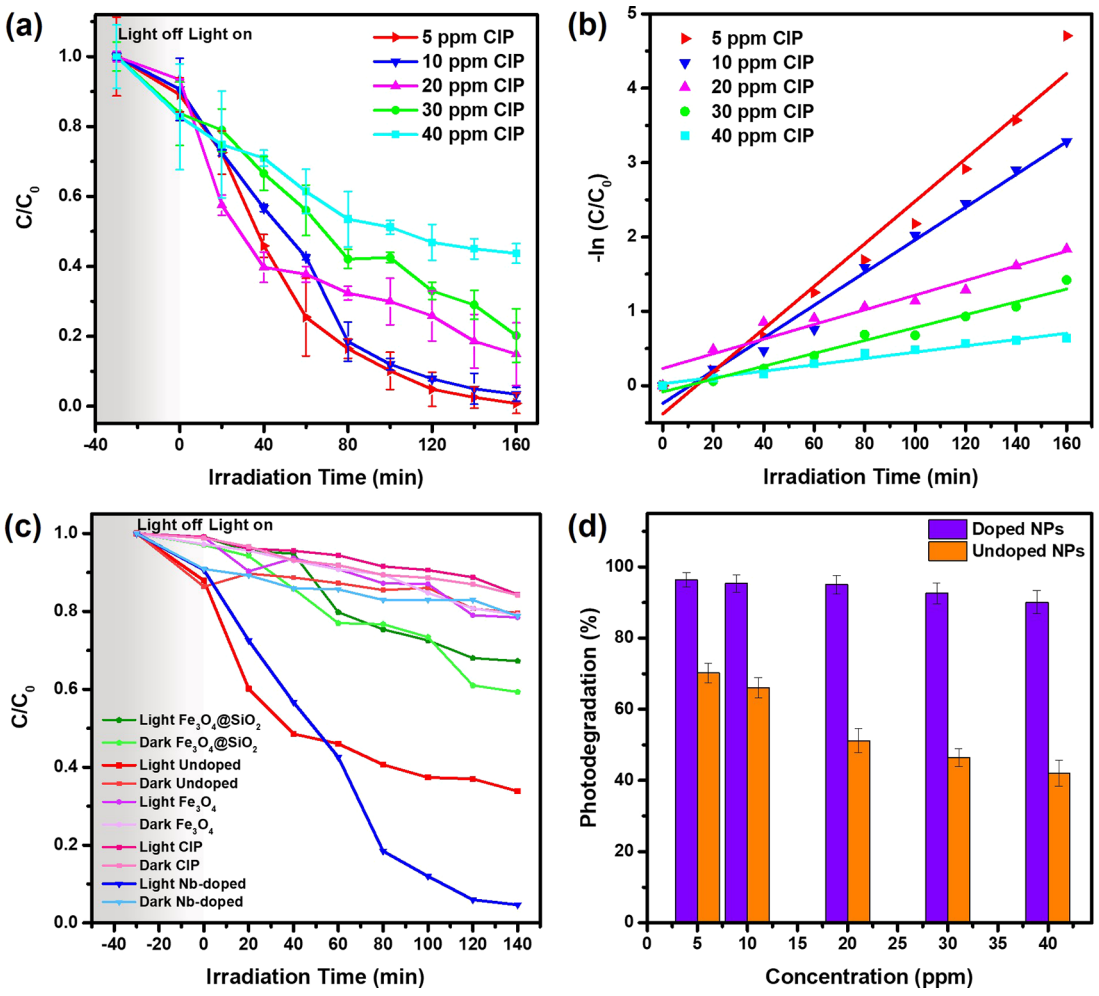

Figure 7. (a) Normalized concentration profiles for the degradation of different CIP concentrations using Fe_3O_4@SiO_2@Nb-TiO_2 NPs. (b) Fitted kinetic degradation curves for various CIP concentrations using Fe_3O_4@SiO_2@Nb-TiO_2 NPs. (c) Normalized CIP concentration profiles for various synthesized NPs under visible light and dark conditions, with initial CIP concentration of 5 ppm. (d) Photodegradation percentages of various CIP concentrations using doped and undoped NPs.

significant changes in dissolution behavior. To provide a more comprehensive evaluation, the experimental duration was extended to 24 h, which confirmed that dissolution remained minimal relative to the total catalyst concentration.

Figure 6 depicts the dissolution behavior of Fe, Ti, and Nb for Fe_3O_4@SiO_2@Nb-TiO_2 NPs under various pH conditions, both with and without visible-light irradiation after 24 h, to evaluate their stability for potential applications in photocatalytic water treatment under different conditions. In the absence of visible light (see Figure 6a), the NPs exhibited stability with minimal dissolution (below 5 ppm), observed only for Fe and Ti ions under extreme acidic (pH 3) and basic (pH 13) conditions. Light irradiation (see Figure 6b) had negligible effects on overall dissolution trends, with minor variations compared to conditions without light. Under both conditions, Fe dissolution was highest at acidic pH, Ti dissolution peaked under alkaline conditions (pH 10), and Nb dissolution remained insignificant across all pH levels. Although Fe ion dissolution reached approximately 4 ppm under strongly acidic conditions (pH 3), this level was observed only under conditions that are not representative of typical environmental scenarios. At near-neutral pH, Fe dissolution was substantially lower, consistent with the limited solubility of the composite material. According to WHO guidelines, no health-based limit is established for iron in drinking water, as concentrations up to 1−3 mg/L are generally not considered toxic due to iron's low toxicity and nutritional relevance.[67] Therefore, the levels of Fe ions observed in this study, particularly under environmentally relevant pH conditions, are unlikely to pose a significant risk to human health or aquatic ecosystems. These findings emphasize the critical role of pH in dissolution behavior and highlight the importance of light stability for optimizing the performance of photocatalysts in water treatment applications.

Photocatalytic Performance of Nanoparticles: Ciprofloxacin Degradation. A detailed analysis of the photocatalytic degradation of CIP under various experimental conditions using both doped and undoped NPs is provided in Figure 7. The degradation of CIP was monitored by measuring its absorbance at the maximum absorption wavelength (270 nm) using UV−vis spectroscopy. Prior to visible-light exposure, the NPs were stirred in the dark with CIP solutions for 30 min to establish adsorption−desorption equilibrium. Control experiments conducted without a photocatalyst and without light irradiation (Figure S6) revealed minimal degradation of CIP (∼16%), confirming the limited contribution of photolysis and adsorption to the overall degradation process. A preliminary experiment with 5 ppm of

https://doi.org/10.1021/acsanm.5c03103
ACS Appl. Nano Mater. 2025, 8, 22540−22552

CIP was conducted to determine the optimal catalyst concentration, which was established as 100 mg for all subsequent experiments.

Figure 7a displays the normalized CIP concentration over 160 min for various initial CIP concentrations. As anticipated, higher initial CIP concentrations correspond to lower degradation efficiencies when a constant catalyst amount was used. The Nb-doped Fe_3O_4@SiO_2@TiO_2 NPs achieved CIP photodegradation of 96, 95, 95, 94, and 90% for initial CIP concentrations of 5, 10, 20, 30, and 40 ppm, respectively. These results significantly outperformed Nb-undoped Fe_3O_4@SiO_2@TiO_2 NPs, which exhibited degradation rates of 70, 66, 51, 46, and 42% under the same conditions and visible-light exposure (see Figure S6). This enhanced performance is attributed to improved electron−hole separation and greater radical generation enabled by Nb doping.

Figure 7b presents the fitted kinetic degradation curves for the different CIP concentrations, demonstrating that the pseudo-first-order kinetics model effectively describes the degradation rates of CIP. As shown in Table S2, the experimental data showed a good fit to the pseudo-first-order kinetics model, with regression coefficient (R^2 values) close to 1. While R^2 values slightly decreased at higher CIP concentrations, they consistently remained above 0.93. In addition, the photodegradation rate decreased with increasing CIP concentration, which is attributed to reduced light penetration and photon absorption by the catalyst at higher CIP concentrations.[68] Figure 7c further compares the photocatalytic activity of Fe_3O_4, Fe_3O_4@SiO_2, Fe_3O_4@SiO_2@TiO_2, and Fe_3O_4@SiO_2@Nb-TiO_2 NPs under light and dark conditions. Only the doped NPs achieved full degradation under visible light, confirming the positive role of Nb incorporation in enhancing photocatalytic activity.

Figure 7d illustrates the photodegradation percentages for various CIP concentrations, showing complete degradation of 5 and 10 ppm CIP within 180 min, while 20, 30, and 40 ppm required up to 280 min for complete degradation (see Figure S6). These findings highlight the superior photocatalytic performance of Fe_3O_4@SiO_2@Nb-TiO_2 NPs, emphasizing the improvement achieved through Nb doping. This enhancement is consistent with previous studies reporting improved performance of magnetic TiO_2-based photocatalysts (Table S3). The observed performance enhancement is attributed to the narrow bandgap, enabling visible-light absorption and reduced electron−hole recombination rate facilitated by Nb doping.

Reusability of Nanoparticles. The reusability of Fe_3O_4@SiO_2@Nb-TiO_2 NPs was evaluated to determine their potential for long-term use in removing CIP from water. Given that antibiotics like CIP are frequently detected in water systems at concentrations of 28−31 ppm, a concentration of 30 ppm was used for reusability cycle studies.[17] The experiments demonstrated that the NPs, owing to their magnetic core−shell structure, can be rapidly separated using an external magnetic field and easily redispersed, enabling their reuse. Over five consecutive cycles, the CIP photodegradation declined from 94% in the first cycle to 77% in the fifth cycle (see Figure 8). This decline in efficiency is likely attributed to several factors such as the minor loss of Fe and Ti ions, surface obstruction, structural degradation, and NP aggregation over multiple cycles. However, the catalyst loss was minimal, with only 13 mg of the initial 100 mg being lost, indicating that the reduction in CIP degradation was primarily due to this minor catalyst loss rather than a loss in intrinsic NP activity. The slightly acidic pH of the solution may have contributed to the ion leaching observed.

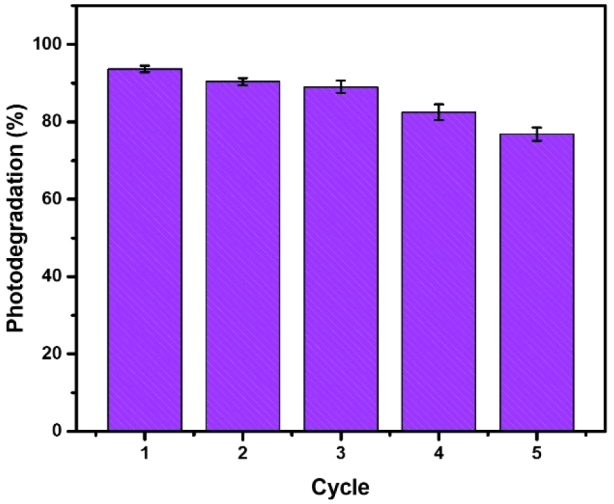

Figure 8. Reusability test for the photocatalytic degradation of CIP by Fe_3O_4@SiO_2@Nb-TiO_2 NPs under visible-light irradiation. Experimental conditions: CIP concentration = 30 ppm, catalyst dosage = 100 mg, reaction time = 220 min. The error bars represent the standard deviations derived from three independent experimental replicates conducted for each cycle.

The Fe_3O_4@SiO_2@Nb-TiO_2 NPs demonstrated superior reusability compared to similar catalysts reported in the literature (Table S3). While other heterogeneous photocatalysts based on graphene oxide or metal−organic frameworks show variable removal efficiencies (typically 60−92%) and maintain activity over five reuse cycles, the current system offers comparable or improved reusability with consistent performance under visible-light irradiation.[69,70] In contrast, some UV-active systems rely on energy-intensive light sources and might require longer irradiation times to achieve similar degradation levels under visible light. Despite a modest decline in efficiency, the Fe_3O_4@SiO_2@Nb-TiO_2 NPs sustained high activity across five cycles (see Figure 8). Simple rinsing between cycles effectively removed residual contaminants without the need for extensive drying steps, thereby enabling faster turnaround times overall, while preserving the NPs' structure, active surface sites, and preventing aggregation typically caused by drying. This straightforward process contributed to the maintenance of catalytic activity above 76% after five cycles. These results confirm the high efficiency, cost-effectiveness, and stable degradation performance of Fe_3O_4@SiO_2@Nb-TiO_2 NPs for water remediation, with minimal loss of photocatalytic activity over multiple reuse cycles.

CONCLUSIONS

This study successfully synthesized and applied Fe_3O_4@SiO_2@Nb-TiO_2 NPs as highly efficient photocatalysts for the degradation of CIP under visible-light irradiation. The NPs, composed of a magnetic Fe_3O_4 core, a silica shell, and a Nb-doped TiO_2 coating, exhibited superior photocatalytic activity, ferrimagnetic behavior, and excellent reusability. Structural and spectroscopic analyses confirmed the successful incorporation of Nb into the TiO_2 lattice, leading to a reduced bandgap energy of 2.67 eV and a decreased electron−hole recombina-

https://doi.org/10.1021/acsanm.5c03103
ACS Appl. Nano Mater. 2025, 8, 22540−22552

tion rate, thereby boosting photocatalytic efficiency. Photocatalytic experiments demonstrated CIP photodegradation ranging from 99 to 96% for initial concentrations between 5 and 40 ppm, with complete degradation achieved within 280 min for higher concentrations. The NPs retained their photocatalytic activity over five reuse cycles, with CIP degradation declining moderately from 94 to 76%, highlighting their durability and stability. Additionally, the ferrimagnetic properties of the dual shell photocatalyst (M_S of 19 emu/g) enabled rapid recovery and reuse with minimal efficiency loss. These findings highlight the potential of Fe_3O_4@SiO_2@Nb-TiO_2 NPs as sustainable and eco-friendly solutions for addressing antibiotic contamination challenge in water systems. By integrating magnetic nanotechnology with advanced photocatalytic properties, this study contributes to the development of recoverable and efficient materials for water treatment, paving the way for future applications in environmental remediation and public health protection.

■ ASSOCIATED CONTENT

Supporting Information

The Supporting Information is available free of charge at https://pubs.acs.org/doi/10.1021/acsanm.5c03103.

Distributions for Fe_3O_4, Fe_3O_4@SiO_2, and Fe_3O_4@SiO_2@Nb-TiO_2 NPs (Figure S1); elemental K-factors and weight percentages (wt %) determined by EDS analysis for Fe_3O_4@SiO_2@Nb-TiO_2 NPs (Table S1); XPS survey spectrum of Fe_3O_4@SiO_2@Nb-TiO_2 NPs (Figure S2); high-resolution XPS spectra for Fe_3O_4@SiO_2@TiO_2 NPs (Figure S3); XRD, TEM, and EDX for Fe_3O_4@TiO_2 and Fe_3O_4@Nb-TiO_2 NPs (Figure S4); diffuse reflectance spectra showing optical absorption of core and core−shell NPs and transformed reflectance spectrum for doped and undoped NPs (Figure S5); CIP concentration over time using Nb-doped and undoped NPs at different initial concentrations (Figure S6); rate constant of Fe_3O_4@SiO_2@Nb-TiO_2 NPs for CIP degradation at different concentrations (Table S2); performance comparison of the developed magnetic TiO catalyst with reported catalysts for CIP degradation (Table S3) (PDF)

■ AUTHOR INFORMATION

Corresponding Authors

T. Randall Lee − *Department of Chemistry and the Texas Center for Superconductivity, University of Houston, Houston, Texas 77204, United States;* orcid.org/0000-0001-9584-8861; Email: trlee@uh.edu

Debora F. Rodrigues − *Department of Environmental Engineering and Earth Science, Clemson University, Clemson, South Carolina 29634, United States;* orcid.org/0000-0002-3124-1443; Email: dfrodri@clemson.edu

Authors

Melissa Ariza Gonzalez − *Department of Chemistry and the Texas Center for Superconductivity, University of Houston, Houston, Texas 77204, United States;* orcid.org/0009-0009-7900-5835

Minh Dang Nguyen − *Department of Chemistry and the Texas Center for Superconductivity, University of Houston, Houston, Texas 77204, United States;* orcid.org/0000-0002-2569-8279

Quoc Minh Tran − *Department of Chemistry and the Texas Center for Superconductivity, University of Houston, Houston, Texas 77204, United States;* orcid.org/0009-0006-8244-3236

Supawitch Hoijang − *Department of Chemistry and the Texas Center for Superconductivity, University of Houston, Houston, Texas 77204, United States;* orcid.org/0000-0002-0061-5166

Pailinrut Chinwangso − *Department of Chemistry and the Texas Center for Superconductivity, University of Houston, Houston, Texas 77204, United States;* orcid.org/0009-0001-0691-8969

Francisco C. Robles Hernandez − *College of Engineering, Division of Technology, University of Houston, Houston, Texas 77204, United States*

Complete contact information is available at: https://pubs.acs.org/10.1021/acsanm.5c03103

Notes

The authors declare no competing financial interest.

■ ACKNOWLEDGMENTS

T.R.L. thanks the Air Force Office of Scientific Research (AFOSR FA9550-23-1-0581; 23RT0567) and the Robert A. Welch Foundation (Grant Nos. V-E-0001 and E-1320) for generous financial support.

■ REFERENCES

(1) Polianciuc, S. I.; Gurzău, A. E.; Kiss, B.; Ştefan, M. G.; Loghin, F. Antibiotics in the Environment: Causes and Consequences. *Med. Pharm. Rep.* **2020**, *93*, 231−240.

(2) Patel, M.; Kumar, R.; Kishor, K.; Mlsna, T.; Pittman, C. U., Jr.; Mohan, D. Pharmaceuticals of Emerging Concern in Aquatic Systems: Chemistry, Occurrence, Effects, and Removal Methods. *Chem. Rev.* **2019**, *119*, 3510−3673.

(3) US Environmental Protection Agency *Contaminants of Emerging Concern including Pharmaceuticals and Personal Care Products*. https://www.epa.gov/wqc/contaminants-emerging-concern-including-pharmaceuticals-and-personal-care-products (accessed 29 August 2024).

(4) Ben, Y.; Fu, C.; Hu, M.; Liu, L.; Wong, M. H.; Zheng, C. Human Health Risk Assessment of Antibiotic Resistance Associated with Antibiotic Residues in the Environment: A Review. *Environ. Res.* **2019**, *169*, 483−493.

(5) Alam, M.-U.; Ferdous, S.; Ercumen, A.; Lin, A.; Kamal, A.; Luies, S. K.; Sharior, F.; Khan, R.; Rahman, M. Z.; Parvez, S. M.; Amin, N.; Tadesse, B. T.; Moushomi, N. A.; Hasan, R.; Taneja, N.; Islam, M. A.; Rahman, M. Effective Treatment Strategies for the Removal of Antibiotic-Resistant Bacteria, Antibiotic-Resistance Genes, and Antibiotic Residues in the Effluent From Wastewater Treatment Plants Receiving Municipal, Hospital, and Domestic Wastewater: Protocol for a Systematic Review. *JMIR Res. Protoc.* **2021**, *10*, No. e33365.

(6) Okoye, C. O.; Nyaruaba, R.; Ita, R. E.; Okon, S. U.; Addey, C. I.; Ebido, C. C.; Opabunmi, A. O.; Okeke, E. S.; Chukwudozie, K. I. Antibiotic Resistance in the Aquatic Environment: Analytical Techniques and Interactive Impact of Emerging Contaminants. *Environ. Toxicol. Pharmacol.* **2022**, *96*, 103995.

(7) Khalid, S.; Shahid, M.; Natasha, N.; Bibi, I.; Sarwar, T.; H, A.; Niazi, N. K. A Review of Environmental Contamination and Health Risk Assessment of Wastewater Use for Crop Irrigation with a Focus on Low and High-Income Countries. *Int. J. Environ. Res. Public Health* **2018**, *15*, 895.

(8) Gomes, I. B.; Maillard, J.-Y.; Simões, L. C.; Simões, M. Emerging Contaminants Affect the Microbiome of Water Systems—Strategies for Their Mitigation. *Npj Clean Water* **2020**, *3*, 39.

(9) Baralla, E.; Demontis, M. P.; Dessì, F.; Varoni, M. V. An Overview of Antibiotics as Emerging Contaminants: Occurrence in Bivalves as Biomonitoring Organisms. *Anim. Open Access J. MDPI* **2021**, *11*, 3239.
(10) Zhen, X.; Lundborg, C. S.; Sun, X.; Hu, X.; Dong, H. Economic Burden of Antibiotic Resistance in ESKAPE Organisms: A Systematic Review. *Antimicrob. Resist. Infect. Control* **2019**, *8*, 137.
(11) Kumar, M.; Ram, B.; Honda, R.; Poopipattana, C.; Canh, V. D.; Chaminda, T.; Furumai, H. Concurrence of Antibiotic Resistant Bacteria (ARB), Viruses, Pharmaceuticals and Personal Care Products (PPCPs) in Ambient Waters of Guwahati; Urban Vulnerability and Resilience Perspective. *Sci. Total Environ.* **2019**, *693*, 133640.
(12) National Academies of Sciences, E.; Division, H. and M.; Practice, B. on P. H. and P. H.; States, C. on the L.-T. H. and E. E. of A. R. in the U. The Health and Economic Burden of Resistance. In *Combating Antimicrobial Resistance And Protecting The Miracle Of Modern Medicine*, Palmer, G. H.; Buckley, G. J. Eds.; National Academies Press: (US), 2021.
(13) Murray, C. J. L.; Ikuta, K. S.; Sharara, F.; Swetschinski, L.; Aguilar, G. R.; Gray, A.; Han, C.; Bisignano, C.; Rao, P.; Wool, E.; et al. Global Burden of Bacterial Antimicrobial Resistance in 2019: A Systematic Analysis. *Lancet* **2022**, *399*, 629−655.
(14) World Health Organization *Model List of Essential Medicines - 23rd list, 2023*. https://www.who.int/publications/i/item/WHO-MHP-HPS-EML-2023.02 (accessed 04 November 2024).
(15) Thai, T.; Salisbury, B. H.; Zito, P. M. Ciprofloxacin. In *StatPearls*; Statpearls Publishing: treasure Island (FL), 2024.
(16) Picó, Y.; Andreu, V. Fluoroquinolones in Soil−Risks and Challenges. *Anal. Bioanal. Chem.* **2007**, *387*, 1287−1299.
(17) Bhagat, C.; Kumar, M.; Tyagi, V. K.; Mohapatra, P. K. Proclivities for Prevalence and Treatment of Antibiotics in the Ambient Water: A Review. *Npj Clean Water* **2020**, *3*, 42.
(18) World Health Organization *Global antimicrobial resistance and use surveillance system (GLASS) report: 2022*. https://www.who.int/publications-detail-redirect/9789240062702 (accessed 30 January 2024).
(19) Singh, B. J.; Chakraborty, A.; Sehgal, R. A Systematic Review of Industrial Wastewater Management: Evaluating Challenges and Enablers. *J. Environ. Manage* **2023**, *348*, 119230.
(20) Manasa, M.; Chandewar, P. R.; Mahalingam, H. Photocatalytic Degradation of Ciprofloxacin & Norfloxacin and Disinfection Studies under Solar Light Using Boron & Cerium Doped TiO_2 Catalysts Synthesized by Green EDTA-Citrate Method. *Catal. Today* **2021**, *375*, 522−536.
(21) Hayder, I.; Qazi, I.; Awan, M. A.; A, M.; Khan, M. A.; Turabi, A. Degradation and Inactivation of Ciprofloxacin by Photocatalysis using TiO_2 Nanoparticles. *J. Appl. Pharm.* **2012**, *4*, 45−55.
(22) Martins, P.; Kappert, S.; Nga Le, H.; Sebastian, V.; Kühn, K.; Alves, M.; Pereira, L.; Cuniberti, G.; Melle-Franco, M.; Lanceros-Méndez, S. Enhanced Photocatalytic Activity of Au/TiO_2 Nanoparticles against Ciprofloxacin. *Catalysts* **2020**, *10*, 234.
(23) Van Doorslaer, X.; Demeestere, K.; Heynderickx, P. M.; Van Langenhove, H.; Dewulf, J. UV-A and UV-C Induced Photolytic and Photocatalytic Degradation of Aqueous Ciprofloxacin and Moxifloxacin: Reaction Kinetics and Role of Adsorption. *Appl. Catal., B* **2011**, *101*, 540−547.
(24) Chen, D.; Cheng, Y.; Zhou, N.; Chen, P.; Wang, Y.; Li, K.; Huo, S.; Cheng, P.; Peng, P.; Zhang, R.; Wang, L.; Liu, H.; Liu, Y.; Ruan, R. Photocatalytic Degradation of Organic Pollutants Using TiO_2 -Based Photocatalysts: A Review. *J. Cleaner Prod.* **2020**, *268*, 121725.
(25) Li, R.; Li, T.; Zhou, Q. Impact of Titanium Dioxide (TiO_2) Modification on Its Application to Pollution Treatment—A Review. *Catalysts* **2020**, *10*, 804.
(26) Etacheri, V.; Di Valentin, C.; Schneider, J.; Bahnemann, D.; Pillai, S. C. Visible-Light Activation of TiO_2 Photocatalysts: Advances in Theory and Experiments. *J. Photochem. Photobiol. C Photochem. Rev.* **2015**, *25*, 1−29.
(27) Aba-Guevara, C. G.; Medina-Ramírez, I. E.; Hernández-Ramírez, A.; Jáuregui-Rincón, J.; Lozano-Álvarez, J. A.; Rodríguez-López, J. L. Comparison of Two Synthesis Methods on the Preparation of Fe, N-Co-Doped TiO_2 Materials for Degradation of Pharmaceutical Compounds under Visible Light. *Ceram. Int.* **2017**, *43*, 5068−5079.
(28) Kaushik, R.; Samal, P. K.; Halder, A. Degradation of Fluoroquinolone-Based Pollutants and Bacterial Inactivation by Visible-Light-Active Aluminum-Doped TiO_2 Nanoflakes. *ACS Appl. Nano Mater.* **2019**, *2*, 7898−7909.
(29) Huang, X.; Yang, W.; Zhang, G.; Yan, L.; Zhang, Y.; Jiang, A.; Xu, H.; Zhou, M.; Liu, Z.; Tang, H.; Dionysiou, D. D. Alternative Synthesis of Nitrogen and Carbon Co-Doped TiO_2 for Removing Fluoroquinolone Antibiotics in Water under Visible Light. *Catal. Today* **2021**, *361*, 11−16.
(30) Aragaw, T. A.; Bogale, F. M.; Aragaw, B. A. Iron-Based Nanoparticles in Wastewater Treatment: A Review on Synthesis Methods, Applications, and Removal Mechanisms. *J. Saudi Chem. Soc.* **2021**, *25*, 101280.
(31) Nguyen, M. D.; Tran, H.-V.; Xu, S.; Lee, T. R. Fe_3O_4 Nanoparticles: Structures, Synthesis, Magnetic Properties, Surface Functionalization, and Emerging Applications. *Appl. Sci.* **2021**, *11*, 11301.
(32) Zhu, N.; Ji, H.; Yu, P.; Niu, J.; Farooq, M. U.; Akram, M. W.; Udego, I. O.; Li, H.; Niu, X. Surface Modification of Magnetic Iron Oxide Nanoparticles. *Nanomaterials* **2018**, *8*, 810.
(33) Kolhatkar, A. G.; Chen, Y.-T.; Chinwangso, P.; Nekrashevich, I.; Dannangoda, G. C.; Singh, A.; Jamison, A. C.; Zenasni, O.; Rusakova, I. A.; Martirosyan, K. S.; Litvinov, D.; Xu, S.; Willson, R. C.; Lee, T. R. Magnetic Sensing Potential of Fe_3O_4 Nanocubes Exceeds That of Fe_3O_4 Nanospheres. *ACS Omega* **2017**, *2*, 8010−8019.
(34) Nguyen, M. D.; Hoijang, S.; Fuller, M.; Deng, L.; Chinwangso, P.; DeTellem, D.; Robles Hernandez, F. C.; Chu, C.-W.; Hadjiev, V. G.; Phan, M.-H.; Lee, T. R. Fine-Tuning the Superparamagnetic Properties of FeO@Fe_3O_4 Core/Shell Nanoparticles and Superclusters by Controlling Size and Shape. *ACS Appl. Mater. Interfaces* **2025**, *17*, 28597−28608.
(35) Issa, B.; Obaidat, I. M.; Albiss, B. A.; Haik, Y. Magnetic Nanoparticles: Surface Effects and Properties Related to Biomedicine Applications. *Int. J. Mol. Sci.* **2013**, *14*, 21266−21305.
(36) Malvindi, M. A.; Matteis, V. D.; Galeone, A.; Brunetti, V.; Anyfantis, G. C.; Athanassiou, A.; Cingolani, R.; Pompa, P. P. Toxicity Assessment of Silica Coated Iron Oxide Nanoparticles and Biocompatibility Improvement by Surface Engineering. *PLoS One* **2014**, *9*, No. e85835.
(37) Krakowiak, R.; Frankowski, R.; Mylkie, K.; Mlynarczyk, D. T.; Ziegler-Borowska, M.; Zgoła-Grześkowiak, A.; Goslinski, T. TiO_2−Fe_3O_4 Composite Systems—Preparation, Physicochemical Characterization, and an Attempt to Explain the Limitations That Arise in Catalytic Applications. *Appl. Sci.* **2022**, *12*, 8826.
(38) Bagwe, R. P.; Hilliard, L. R.; Tan, W. Surface Modification of Silica Nanoparticles to Reduce Aggregation and Non-Specific Binding. *Langmuir* **2006**, *22*, 4357.
(39) Kralj, S.; Makovec, D.; Čampelj, S.; Drofenik, M. Producing Ultra-Thin Silica Coatings on Iron-Oxide Nanoparticles to Improve Their Surface Reactivity. *J. Magn. Magn. Mater.* **2010**, *322*, 1847−1853.
(40) Rivas Rojas, P. C.; Tancredi, P.; Moscoso Londoño, O.; Knobel, M.; Socolovsky, L. M. Tuning Dipolar Magnetic Interactions by Controlling Individual Silica Coating of Iron Oxide Nanoparticles. *J. Magn. Magn. Mater.* **2018**, *451*, 688−696.
(41) Santra, S.; Tapec, R.; Theodoropoulou, N.; Dobson, J.; Hebard, A.; Tan, W. Synthesis and Characterization of Silica-Coated Iron Oxide Nanoparticles in Microemulsion: The Effect of Nonionic Surfactants. *Langmuir* **2001**, *17*, 2900−2906.
(42) Ngo, N. M.; Nguyen, M. D.; Tran, H.-V.; Medhi, R.; Lee, J. M.; Lee, T. R. Photocatalytic Hydrogen Generation by Monodisperse

TiO_2 Nanoparticles Singly and Dually Doped with Niobium and Tantalum. *ACS Appl. Nano Mater.* **2025**, *8*, 4841−4851.
(43) Yan, W.; Liu, X. Niobium-Doped TiO_2: Effect of an Interstitial Oxygen Atom on the Charge State of Niobium. *Inorg. Chem.* **2019**, *58*, 3090−3098.
(44) Lim, J.; Monllor-Satoca, D.; Jang, J. S.; Lee, S.; Choi, W. Visible Light Photocatalysis of Fullerol-Complexed TiO_2 Enhanced by Nb Doping. *Appl. Catal., B* **2014**, *152*−*153*, 233−240.
(45) Qian, X.; Yang, W.; Gao, S.; Xiao, J.; Basu, S.; Yoshimura, A.; Shi, Y.; Meunier, V.; Li, Q. Highly Selective, Defect-Induced Photocatalytic CO_2 Reduction to Acetaldehyde by the Nb-Doped TiO_2 Nanotube Array under Simulated Solar Illumination. *ACS Appl. Mater. Interfaces* **2020**, *12*, 55982−55993.
(46) Nogueira, M. V.; Lustosa, G. M. M. M.; Kobayakawa, Y.; Kogler, W.; Ruiz, M.; Monteiro Filho, E. S.; Zaghete, M. A.; Perazolli, L. A. Nb-Doped TiO_2 Photocatalysts Used to Reduction of CO_2 to Methanol. *Adv. Mater. Sci. Eng.* **2018**, *2018* (1), 7326240.
(47) Kong, L.; Wang, C.; Zheng, H.; Zhang, X.; Liu, Y. Defect-Induced Yellow Color in Nb-Doped TiO_2 and Its Impact on Visible-Light Photocatalysis. *J. Phys. Chem. C* **2015**, *119*, 16623−16632.
(48) Potlog, T.; Dumitriu, P.; Dobromir, M.; Manole, A.; Luca, D. Nb-Doped TiO_2 Thin Films for Photovoltaic Applications. *Mater. Des.* **2015**, *85*, 558−563.
(49) Lee, S.; Noh, J. H.; Han, H. S.; Yim, D. K.; Kim, D. H.; Lee, J.-K.; Kim, J. Y.; Jung, H. S.; Hong, K. S. Nb-Doped TiO_2: A New Compact Layer Material for TiO_2 Dye-Sensitized Solar Cells. *J. Phys. Chem. C* **2009**, *113*, 6878−6882.
(50) Kim, D.; Lee, N.; Park, M.; Kim, B. H.; An, K.; Hyeon, T. Synthesis of Uniform Ferrimagnetic Magnetite Nanocubes. *J. Am. Chem. Soc.* **2009**, *131*, 454−455.
(51) Ding, H. L.; Zhang, Y. X.; Wang, S.; Xu, J. M.; Xu, S. C.; Li, G. H. Fe_3O_4@SiO_2 Core/Shell Nanoparticles: The Silica Coating Regulations with a Single Core for Different Core Sizes and Shell Thicknesses. *Chem. Mater.* **2012**, *24*, 4572−4580.
(52) Lee, J.-W.; Kong, S.; Kim, W.-S.; Kim, J. Preparation and Characterization of SiO_2/TiO_2 Core-Shell Particles with Controlled Shell Thickness. *Mater. Chem. Phys.* **2007**, *106*, 39−44.
(53) Drašinac Pajić, N.; Djinović, P.; Dražić, G.; Grdadolnik, J.; Šket, P.; Cerkovnik, J.; Pintar, A. Structural Stabilization and Characterization of Active Peroxo Species on TiO_2-Nanotube Based Materials in Mild Catalytic Wet Peroxide Oxidation Process. *Appl. Catal. Gen.* **2018**, *562*, 276−283.
(54) Shu, X.; Chen, Y.; Yuan, H.; Gao, S.; Xiao, D. H_2O_2 Sensor Based on the Room-Temperature Phosphorescence of Nano TiO_2/SiO_2 Composite. *Anal. Chem.* **2007**, *79*, 3695−3702.
(55) Santos, E.; Catto, A. C.; Peterline, A. F.; Avansi, W., Jr Transition Metal (Nb and W) Doped TiO_2 Nanostructures: The Role of Metal Doping in Their Photocatalytic Activity and Ozone Gas-Sensing Performance. *Appl. Surf. Sci.* **2022**, *579*, 152146.
(56) Su, H.; Huang, Y.-T.; Chang, Y.-H.; Zhai, P.; Hau, N. Y.; Cheung, P. C. H.; Yeh, W.-T.; Wei, T.-C.; Feng, S.-P. The Synthesis of Nb-Doped TiO_2 Nanoparticles for Improved-Performance Dye Sensitized Solar Cells. *Electrochim. Acta* **2015**, *182*, 230−237.
(57) Kolhatkar, A. G.; Jamison, A. C.; Litvinov, D.; Willson, R. C.; Lee, T. R. Tuning the Magnetic Properties of Nanoparticles. *Int. J. Mol. Sci.* **2013**, *14*, 15977−16009.
(58) Nguyen, M. D.; Deng, L.; Lee, J. M.; Resendez, K. M.; Fuller, M.; Hoijang, S.; Robles-Hernandez, F.; Chu, C.-W.; Litvinov, D.; Hadjiev, V. G.; et al. Magnetic Tunability via Control of Crystallinity and Size in Polycrystalline Iron Oxide Nanoparticles. *Small* **2024**, *20*, 2402940.
(59) Liqiang, J.; Yichun, Q.; Baiqi, W.; Shudan, L.; Baojiang, J.; Libin, Y.; Wei, F.; Honggang, F.; Jiazhong, S. Review of Photoluminescence Performance of Nano-Sized Semiconductor Materials and Its Relationships with Photocatalytic Activity. *Sol. Energy Mater. Sol. Cells* **2006**, *90*, 1773−1787.
(60) Li, N.; Zhang, J.; Tian, Y.; Zhao, J.; Zhang, J.; Zuo, W. Precisely Controlled Fabrication of Magnetic 3D γ-Fe_2O_3@ZnO Core-Shell Photocatalyst with Enhanced Activity: Ciprofloxacin Degradation and Mechanism Insight. *Chem. Eng. J.* **2017**, *308*, 377−385.
(61) Marschall, R. Semiconductor Composites: Strategies for Enhancing Charge Carrier Separation to Improve Photocatalytic Activity. *Adv. Funct. Mater.* **2014**, *24*, 2421−2440.
(62) Teixeira, S.; Mora, H.; Blasse, L.-M.; Martins, P. M.; Carabineiro, S. A. C.; Lanceros-Méndez, S.; Kühn, K.; Cuniberti, G. Photocatalytic Degradation of Recalcitrant Micropollutants by Reusable Fe_3O_4/SiO_2/TiO_2 Particles. *J. Photochem. Photobiol. Chem.* **2017**, *345*, 27−35.
(63) Makuła, P.; Pacia, M.; Macyk, W. How To Correctly Determine the Band Gap Energy of Modified Semiconductor Photocatalysts Based on UV−Vis Spectra. *J. Phys. Chem. Lett.* **2018**, *9*, 6814−6817.
(64) Álvarez, P. M.; Jaramillo, J.; López-Piñero, F.; Plucinski, P. K. Preparation and Characterization of Magnetic TiO_2 Nanoparticles and Their Utilization for the Degradation of Emerging Pollutants in Water. *Appl. Catal., B* **2010**, *100*, 338−345.
(65) Fanourakis, S. K.; Peña-Bahamonde, J.; Rodrigues, D. F. Inorganic Salts and Organic Matter Effects on Nanorod, Nanowire, and Nanoplate MoO_3 Aggregation, Dissolution, and Photocatalysis. *Environ. Sci.: Nano* **2020**, *7*, 3794−3804.
(66) Chen, K.; Dong, W.; Huang, Y.; Wang, F.; Zhou, J. L.; Li, W. Photocatalysis for Sustainable Energy and Environmental Protection in Construction: A Review on Surface Engineering and Emerging Synthesis. *J. Environ. Chem. Eng.* **2025**, *13*, 117529.
(67) World Health Organization *Iron in Drinking Water*. https://cdn.who.int/media/docs/default-source/wash-documents/wash-chemicals/iron-bd.pdf (accessed 08 November 2025).
(68) Ahmadpour, N.; Sayadi, M. H.; Sobhani, S.; Hajiani, M. Photocatalytic Degradation of Model Pharmaceutical Pollutant by Novel Magnetic TiO_2@$ZnFe_2O_4$/Pd Nanocomposite with Enhanced Photocatalytic Activity and Stability under Solar Light Irradiation. *J. Environ. Manage* **2020**, *271*, 110964.
(69) Uruş, S.; Çaylar, M.; Eskalen, H.; Özgan, Ş. Synthesis of GO@Fe_3O_4@TiO_2 Type Organic−Inorganic Nanohybrid Material: Investigation of the Effect of Nanohybrid Doped Liquid Crystal E7 and the Photocatalytic Degradation of Ciprofloxacin. *J. Mater. Sci.: Mater. Electron.* **2022**, *33*, 4314−4329.
(70) Tilgner, D.; Friedrich, M.; Verch, A.; de Jonge, N.; Kempe, R. A Metal−Organic Framework Supported Nonprecious Metal Photocatalyst for Visible-Light-Driven Wastewater Treatment. *Chem. Photo. Chem.* **2018**, *2*, 349−352.

https://doi.org/10.1021/acsanm.5c03103
ACS Appl. Nano Mater. 2025, 8, 22540−22552